Contact Deformation of $LiNbO_3$ Single Crystal: Dislocations, Twins and Ferroelectric Domains

Application Note

Sandip Basu and Shijie Wu

Abstract

Reliability of many Lithium niobate — $LiNbO_3$ — optoelectronic devices depends on proper understanding of their deformation behavior under contact stresses that may occur during various fabrication steps. This study addresses this need by using a nanoindentation method to determine the critical shear stress needed for the transition from pure elastic to elastic-plastic deformation. The transition stresses determined during this study are lower than the theoretical shear strength, indicating the presence and distribution of defect nucleation centers those formed during the crystal growth or fabrication processes. We demonstrate here that $(10\bar{1}2)[\bar{1}011]$ twins form underneath the indented region, whereas dislocation based deformation is dominant further away from the center of the indent. Piezo-response force microscopy (PFM) revealed that while the dislocations nucleated during contact loading do not interact with existing ferroelectric domains, the deformation twins near the center of the indent form new domains with inverted polarization.

Introduction

$LiNbO_3$ has important nonlinear optical properties for applications in electro-optic, acousto-optic, and optical storage devices.[1] These crystals are often periodically poled (PPLN) – with P^+ and P^- domains with a period of about 5 to 35 µm – for nonlinear optics applications. Precise knowledge of the mechanical deformation of $LiNbO_3$ under contact loading is a prerequisite for successful manufacturing and operation of these single crystal devices. Despite the importance, very little is available on the elastic-plastic transition and dislocation movement during contact deformation in $LiNbO_3$.

Earlier studies on $LiNbO_3$ single crystals have been limited to mostly uniaxial compression[2] and Vickers microhardness.[3] When single crystals are loaded in uniaxial compression at temperatures >1150°C, $(10\bar{1}2)[\bar{1}011]$ twins form.[2] Within these twins, basal slip is observed. More recently, Park et al.[4] confirmed the existence of this twin system. Recently, researchers have also demonstrated reversible

Agilent Technologies

dislocation motion in $LiNbO_3$ single crystal during cyclic nanoindentation experiments.[5] However, little is known about the effect of mechanical deformation mechanisms — especially twinning and dislocations — on the ferroelectric domains in $LiNbO_3$. Herein, we characterize the formation of twins and dislocation structures during nanoindentation in a (0001) PPLN crystal. In order to characterize the mechanical behavior, we first study the elastic to elastic-plastic transition by spherical nanoindentation. Subsequent characterization of the domain structures were carried out using piezo force microscopy (PFM). Before discussing the particular results for $LiNbO_3$, the following sections briefly review the nanoindentation and atomic force microscopy methods used during this study.

Nanoindentation: Theory and Experimental Details

The nanoindentation experiments on the (0001) PPLN crystal were carried out at room temperature using a G200 NanoIndenter, fitted with a diamond sphero-conical indenter with 1 µm apical radius. The strain rate during loading was kept constant at 0.05/sec. The contact stiffness was measured by applying a harmonic force modulation with the continuous stiffness measurement (CSM) attachment, during the complete loading segment. This method enables measurement of the contact stiffness as a continuous function of displacement during indenting a material. The measured load (P), displacement (h_t) and contact harmonic stiffness (S) were then analyzed according to Hertzian contact mechanics, as discussed below. The contact depth (h_c) was calculated according to the Oliver-Pharr model:[6]

$$h_c = h_t - \varepsilon \frac{P}{S} \quad (1)$$

where, ε is a constant with a value of 0.75 for a spherical indenter. It is important to note here that this equation can be applied in both elastic and elastic-plastic regimes to calculate the contact depth. Once the contact depth was known, the contact radius (a) was calculated as:

$$a = \sqrt{2Rh_c - h_c^2} \quad (2)$$

where, R is the tip radius. According to the theory of elastic contacts,[7] the contact radius is related to the harmonic contact stiffness by:

$$S = 2E^* a \quad (3)$$

where, E^* is the reduced modulus that is a function of both the sample and the tip, and can be expressed as:

$$\frac{1}{E^*} = \frac{1-\nu^2}{E} + \frac{1-\nu_i^2}{E_i} \quad (4)$$

E and ν are Young's modulus and Poisson's ratio, respectively. The subscript 'i' represents the properties of the diamond tip, which has a Young's modulus of 1140 GPa, and a Poisson's ratio of 0.07.

Hence, for the elastic regime, the modulus of the sample can be measured from the slope of an S vs. a curve, which should be linear based on Eqn. 3. Now, the representative 'indentation stress' was calculated as:[8]

$$\sigma = \frac{P}{\pi a^2} \quad (5)$$

A representative 'indentation strain' can also be expressed by:[8]

$$\varepsilon = \frac{a}{R} \quad (6)$$

In the elastic regime, the indentation stress is a linear function of the indentation strain.[7]

$$\frac{P}{\pi a^2} = \frac{4}{3\pi} E^* \left(\frac{a}{R}\right) \quad (7)$$

Note that a rigorous expression of strain for elastic-plastic indentation is still very much a topic of ongoing discussion.

Piezoresponse Force Microscopy (PFM): Theory and Experimental Details

Piezoresponse Force Microscopy (PFM) has become a popular technique for nanoscale characterization of ferroelectric and piezoelectric materials.[9–11] It is based on the converse piezoelectric effect where piezoelectric materials change their dimensions when subjected to an external electric field. The strain S_j developed in a piezoelectric material by the applied electric field E_i is described by the following matrix equation:[12]

$$S_j = d_{ij} E_i \quad (8)$$

where d_{ij} is the piezoelectric coefficient with the unit of m/V. The indices i = 1, 2, 3 and j = 1, 2, 3...6 denotes the direction of the electric field and the tensor component of the strain following the Voigt notation.[13] In general, indices 1, 2, and 3 indicate components along the x, y, and z axis of an orthogonal coordinate system, and indices 4, 5, and 6 indicate shear components of the strain tensor. The axes of the coordinate system are often conveniently aligned with the crystallographic axes of a crystal. In the case of ceramics and thin films, the z axis is usually aligned with the direction of the polarization, or the direction normal to the plane of the film. The piezoelectric coefficient measured along the direction of the applied field is also called the longitudinal piezoelectric constant, and that being perpendicular to the electric field are called transverse piezoelectric constants. Therefore, the longitudinal piezoelectric constant, d_{33}, can be determined by measuring the displacement (Δz) of the piezoelectric material along the direction of the applied field (E_3):

$$\Delta z = d_{33} V \quad (9)$$

assuming $S_3 = \Delta z / z_0$ and $E_3 = V / z_0$, where V is the applied voltage and z_0 is the thickness of the sample. The measured displacement will be positive, i.e.

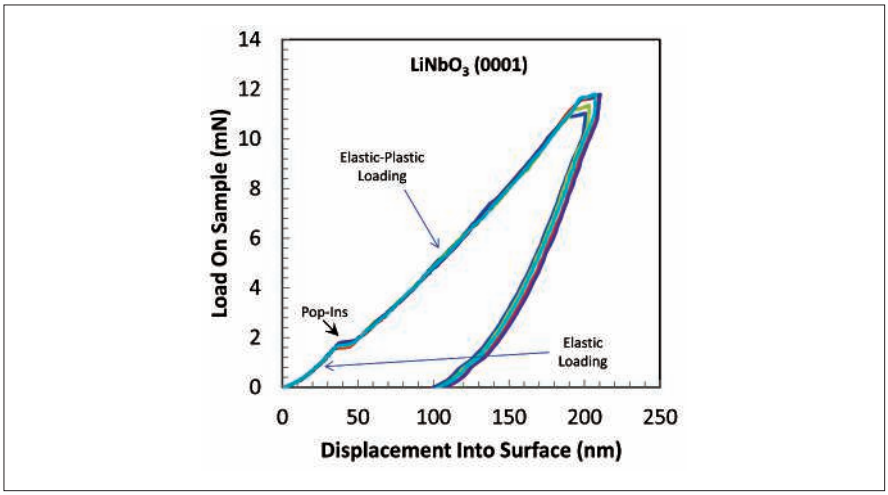

Figure 1. Nanoindentation load-displacement response from 5 different locations on (0001) $LiNbO_3$ surface, indented with a sphero-conical indenter of 1 µm tip radius. Note the distinct pop-in events marking the transition from elastic to elastic-plastic deformation.

expansion, if the polarization direction is parallel to the applied field, and it will be negative if the polarization direction is antiparallel to the applied field.

With PFM, a conductive AFM cantilever is scanned across the surface of a piezoelectric sample in contact mode. The conductive cantilever also serves as the top electrode to provide the polarization field to the sample. The sample can be either connected to a bottom electrode or floating. In the case the sample is connected to a bottom electrode, the electric bias can be applied to the sample as well.

In PFM experiment, an ac voltage modulation, $V = V_{ac}\, cos(\omega t)$, is applied to the conductive AFM tip, the displacement thus measured, according to equation (9), will be

$$\Delta z = d_{33}\, V_{ac}\, cos(\omega t + \phi) \qquad (10)$$

with $\phi = 0$, for P^-
(polarization pointing downwards)
$\phi = \pi$, for P^+
(polarization pointing upwards)

Therefore, when a small ac modulation being added to the applied electric field, the piezoresponse will oscillate in-phase with the ac modulation signal if the polarization is parallel to the field, and out-phase if antiparallel. Consequently a lock-in amplifier can be used to analyze the piezoresponse signal and to determine both the magnitude of the displacement and the polarization direction of the sample. The detection of longitudinal piezoresponse is also called vertical piezoresponse force microscopy (VPFM).

The presence of non-zero transverse piezoelectric constants, e.g. d_{15}, and the possible misalignment of polarization to the applied field due to random crystal orientation, an electric field normal to the surface can also cause in-plane shear deformation. This in-plane shear deformation of the sample will give rise to a torsion-like motion to the AFM cantilever, thus results in a change in the friction signal (or the lateral force signal). In a way similar to VPFM, a lock-in amplifier can be used to detect the in-plane piezoresponse signal ΔL induced by an ac voltage modulation:

$$\Delta L = d_{eff}\, V_{ac}\, cos(\omega t + \phi) \qquad (11)$$

where d_{eff} is the effective in-plane piezoresponse constant, and ϕ is the phase angle related to polarization direction. For antiparallel domains the phase angle will be 180° in difference. The measurement of in-plane piezoresponse is often called lateral piezoresponse force microscopy (LPFM).[14]

In this study, post-indentation topography was examined using a 5600 LS Atomic Force Microscope (AFM). The ferroelectric domains of the indent structure were imaged using PFM capability implemented in the AFM. The conductive cantilever used is a Pt-coated cantilever with a force constant of 2.8 N/m. An ac modulation voltage of 4 volts peak-to-peak at 12 kHz was applied to acquire the PFM signal.

Results and Discussions

The load-displacement response for the 1 µm indentation on the (0001) PPLN clearly exhibits three distinct regimes of deformation — a fully elastic deformation, followed by pop-ins (or, displacement bursts), and subsequent elastic-plastic deformation. The pop-ins represents the transition from elastic to elastic-plastic deformation. So, before the pop-in the deformation is completely linear elastic as discussed in the literature. The elastic modulus can thus be measured from the slope of the contact stiffness vs. contact radius plot as shown in Figure 2a. At 207 ± 2 GPa, the elastic modulus measured from this spherical nanoindentation method is comparable with Berkovich nanoindentation measurement (200 ± 2 GPa) on the same surface.

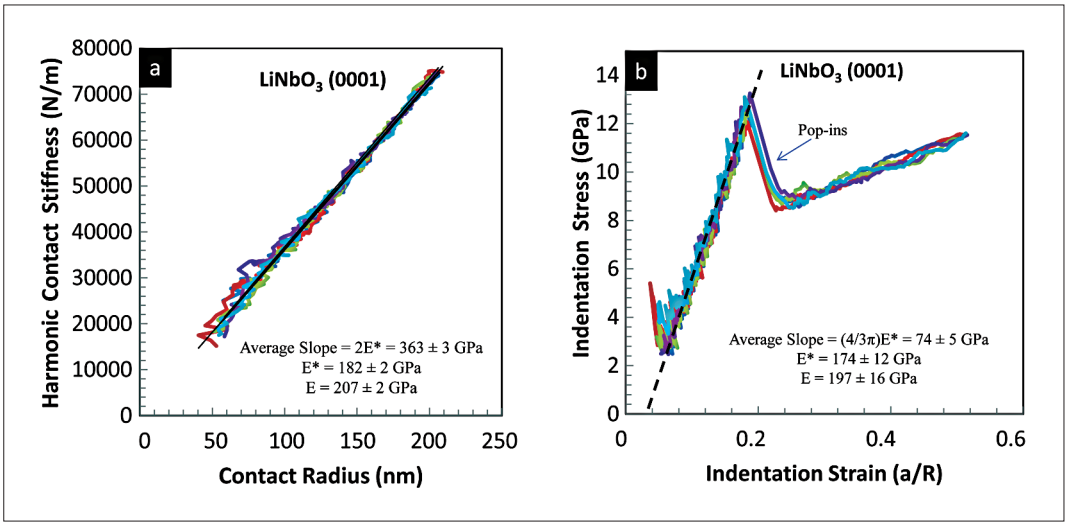

Figure 2. (a) The contact harmonic stiffness as a linear function of contact radius before the pop-in. (b) Indentation stress-strain curves corresponding to the load-displacement response shown in Figure 1. The dotted line represents the linear slope from which the elastic modulus was measured.

The linear elastic behavior is also evident from the indentation stress-strain curve shown in Figure 2b. The elastic modulus measured from the linear slope is 197±16 GPa. The agreement between modulus measurements from different data sets is noteworthy and validates these calculations. Although the stress-strain calculations beyond the maximum pop-in load are debatable, these curves can be extremely useful for comparison between different length scales and different defect population in single crystals.

It is possible to calculate the maximum shear stress under the indenter from:[7]

$$\tau = 0.31\left(\frac{6PE^{*2}}{\pi^3 R^2}\right)^{\frac{1}{3}} \quad (12)$$

The maximum shear stress occurs at a depth of about 0.48 times the contact radius under the contact surface. Figure 3 shows a distribution of the maximum shear stresses during pop-in from 25 measurements. Although the pop-ins occur at a lower stress than the theoretical shear strength of the crystal ($G/2\pi$), this information can be used to monitor the defect population during manufacturing and application of these crystals.

The pop-ins during nanoindentation can be caused by different mechanisms, such as dislocation nucleation and propagation, twinning, phase transformation, etc. However, there may be some relationship between the statistical distribution of maximum shear stresses at pop-ins to the exact deformation mechanism. Therefore, more work is needed to establish such characteristic parameters. With the information from the SEM observations reported in literature,[5] it is reasonable to conclude that in case of $LiNbO_3$ twinning along the $(10\bar{1}2)[\bar{1}011]$ system occurs. From crystallography, these twins form in a triangular pattern,[4] and the number of twin bands increases with increasing load (or, stress) underneath the indenter. Beyond the pop-in, the bending of basal planes also causes dislocations to nucleate and glide further away from the indented region. The interaction between the dislocations may cause the observed

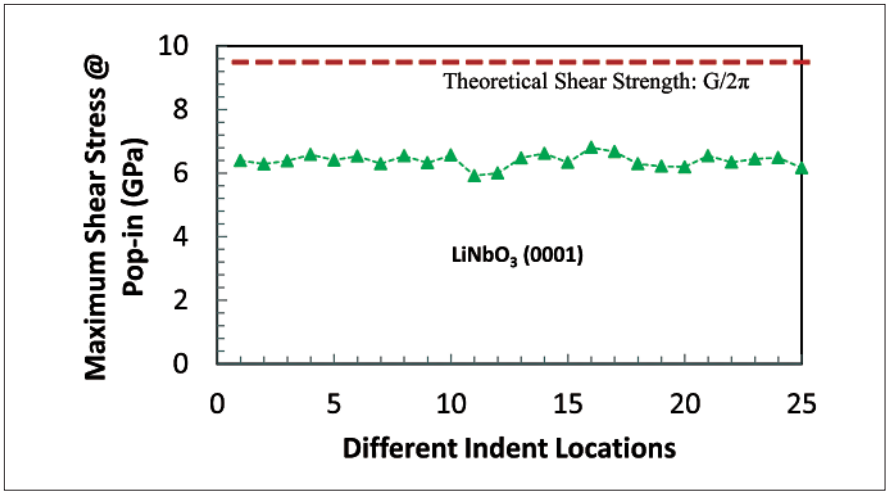

Figure 3. Distribution of maximum shear stress during the pop-in events when (0001) $LiNbO_3$ was indented with a 1μm sphero-conical indenter. The dotted line shows the theoretical shear strength of the material.

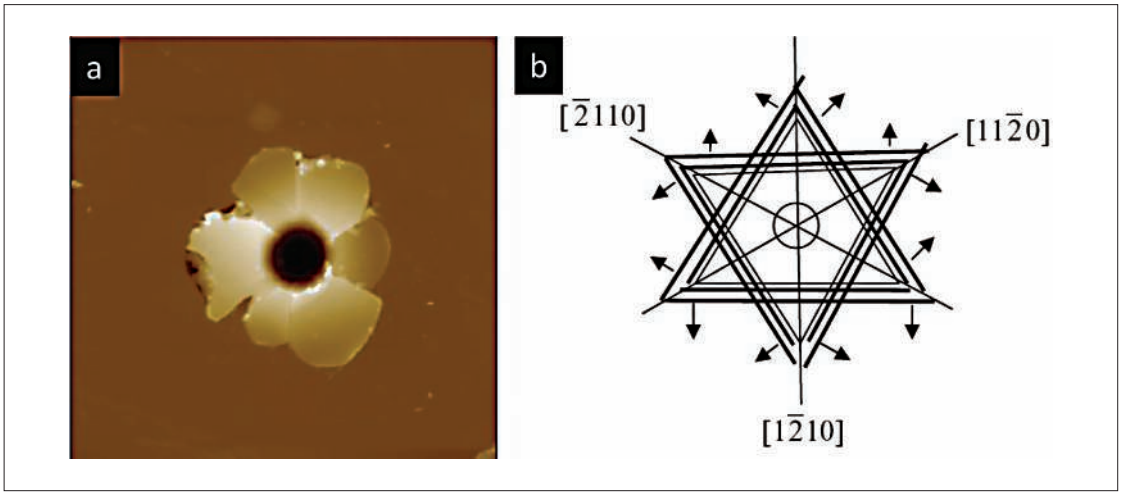

Figure 4. (a) AFM topography of a region indented down to 2µm into the (0001) $LiNbO_3$ surface with a 1µm sphero-conical indenter tip. The scan area is 15µm x 15µm. (b) Schematic showing gliding directions of basal plane dislocations in $LiNbO_3$. Note the hexagonal symmetry matches with the hexagonal pattern of delaminations and pile-up observed in (a).

strain hardening, but more research is needed to understand the nature of interactions.

Besides the elastic modulus, the other objective of this study was to find the relationships between twinning, dislocations and the ferroelectric domains in single crystal PPLN from PFM measurements. Figure 4a shows the topography of a typical location indented to 2µm using the sphero-conical indenter tip. The severe delamination and pile-up around the indent is clearly visible. More interestingly, the deformation features exhibit a hexagonal symmetry, strongly suggesting that the primary deformation mechanism around the indented region is dislocation-based. Being a hexagonal crystal, the (0001) is a favorable slip plane in $LiNbO_3$, and dislocations can glide along the [11$\bar{2}$0] directions, as shown in the schematic in Figure 4b.

The PFM images of the same location reveal that part of the deformed region due to the indentation crossed an existing domain boundary in the PPLN crystal. The sharp boundary between the P^+ (brighter region, orientation: normal-upward) and P^- (darker region, orientation: normal-downward) ferroelectric domains is evident in the PFM amplitude image in Figure 5a, but more clearly visible in the PFM phase image in Figure 5b. The dislocations,

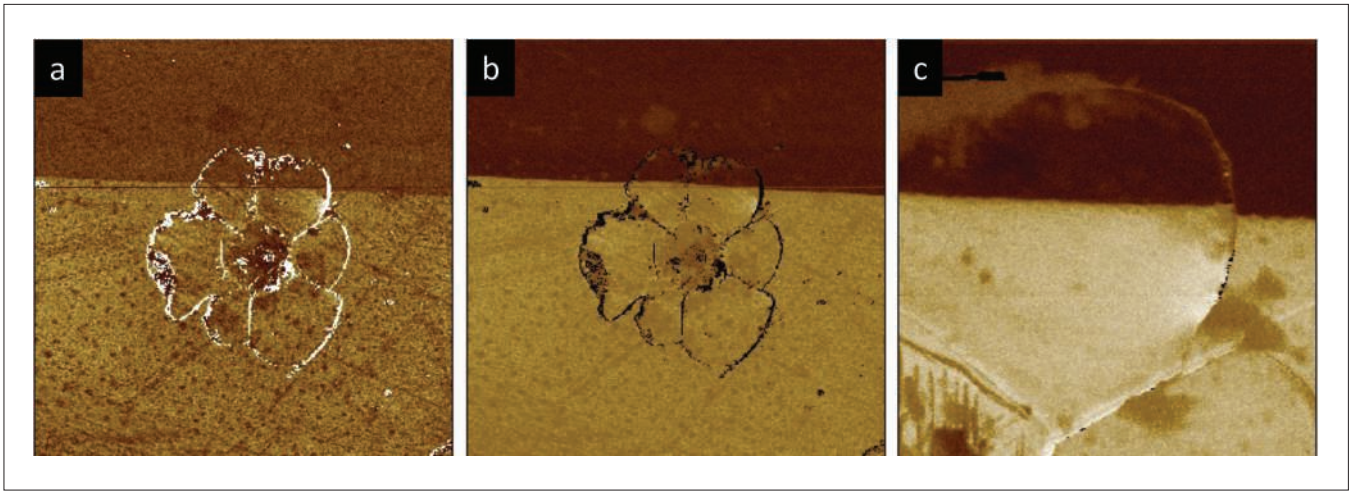

Figure 5. Images — corresponding to Figure 4 — of (a) PFM amplitude, and (b) PFM phase, showing a 180O domain boundary in the PPLN crystal. Note that the dislocation-based deformation region crosses a domain boundary without affecting the domain structure. (c) Magnified (3µm square) PFM phase image of the deformation region crossing the ferroelectric domain boundary.

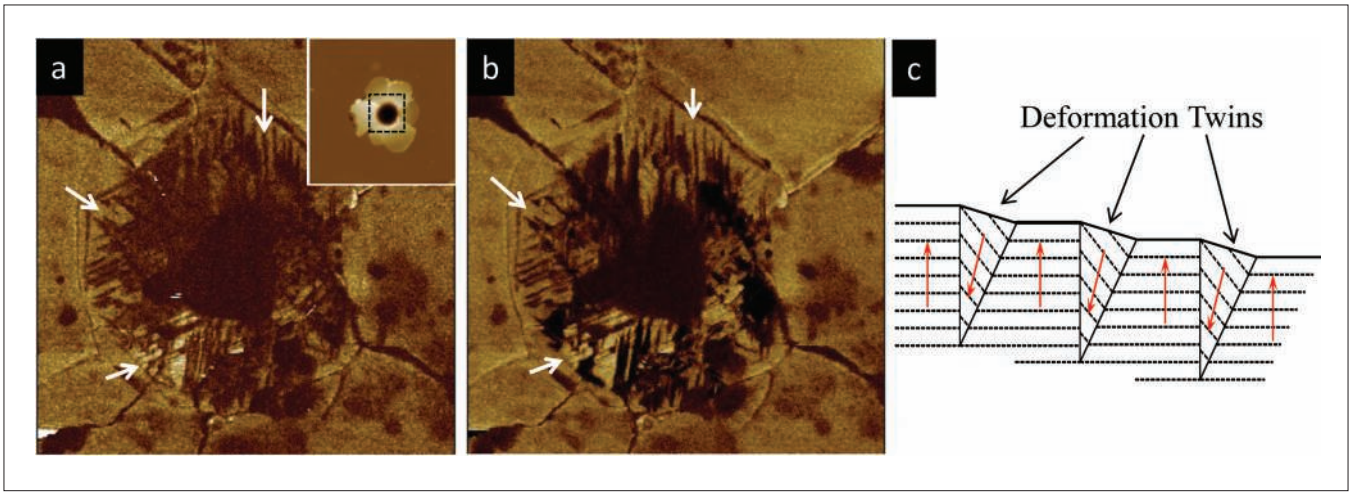

Figure 6. (a) PFM amplitude, and (b) PFM phase images showing formation of deformation twins inside the indented region (marked by dotted square in the inset), with alternate +ve and –ve ferroelectric domains (white arrows). The scan area is 4 µm x 4 µm. (c) A schematic showing orientation of (0001) planes (dashed lines) and the ferroelectric domains (red arrows) at a $(10\bar{1}2)[\bar{1}011]$ deformation twin formed during nanoindentation.

mostly basal, that are nucleated due to indentation stress, move away from the indented region causing bending and eventually delamination of the top layer. It is surprising that even the dislocations in the delaminated region did not affect the existing domain structure of the PPLN crystal (Figure 5c), indicating that the basal dislocations have no significant effect on ferroelectric polarization in $LiNbO_3$.

While dislocations dominate the deformation further away from the center of the indent, twinning occurs close to the center of the indent when the contact shear stress reaches the critical value for the crystal. It has also been discussed in literature that the ferroelectric domains can be related to deformation twins in $LiNbO_3$. The PFM amplitude and phase images in Figure 6 clearly show the alternate ferroelectric domains that formed along the twins (white arrows).

As shown in Figure 5a, the region investigated in Figure 6 lies completely inside an existing P^+ domain of the PPLN. The similarity in contrast in the bright bands along the twins with the surrounding area suggests that the orientation of the domains in these regions is still P^+. However, the alternate darker bands along the twins indicate domains with downward orientation. By comparing the differences in phase contrast between brighter and darker regions in Figs. 5b and 6b, it can be inferred that the darker ferroelectric domains along the twins are not exactly normal to the (0001) plane. Rather these switched domains are inclined at an angle. This inclined nature of these domains is most likely due to the change in crystallographic orientation inside the twinned region, as shown in the schematic in Figure 6c. More work must be done to determine the exact orientation of the alternate ferroelectric domains that form during contact loading of $LiNbO_3$ single crystal.

Summary and Conclusions

A combined nanoindentation and AFM investigation showed that twinning and dislocation motion are two major deformation mechanisms under contact loading in periodically poled (0001) $LiNbO_3$. The piezo-response force microscopy (PFM) reveals that basal plane dislocations in $LiNbO_3$ do not affect ferroelectric domain boundaries. On the other hand, the ferroelectric domains can be correlated with deformation twins that form during contact loading of the crystal. These results are important for improved production and failure analysis of PPLN crystals.

References

1 Weis, R.S., Gaylord, T.K. Lithium niobate: Summary of physical properties and crystal structure. *Appl. Phys. A* **37,** 191–203, doi:10.1007/bf00614817 (1985).

2 Vere, A.W. Mechanical twinning and crack nucleation in lithium niobate. *Journal of Materials Science* **3,** 617–621, doi:10.1007/bf00757908 (1968).

3 Subhadra, K.G., Kishan Rao, K., Sirdeshmukh, D.B. Systematic hardness studies on lithium niobate crystals. *Bull Mater Sci* **23,** 147–150, doi:10.1007/bf02706557 (2000).

4 Park, B.M., Kitamura, K., Furukawa, Y., Ji, Y. Relation between Mechanical Twinning and Cracking in Stoichiometric Lithium Niobate Single Crystals. *Journal of the American Ceramic Society* **80,** 2689–2692, doi:10.1111/j.1151-2916.1997.tb03174.x (1997).

5 Basu, S., Zhou, A., Barsoum, M.W. Reversible dislocation motion under contact loading in LiNbO3 single crystal. *Journal of Materials Research* **23,** 1334-1338, doi:doi:10.1557/JMR.2008.0150 (2008).

6 Oliver, W.C., Pharr, G.M. An improved technique for determining hardness and elastic modulus using load and displacement sensing indentation experiments. *Journal of Materials Research* **7,** 1564–1583, doi:doi:10.1557/JMR.1992.1564 (1992).

7 Johnson, K.L. *Contact Mechanics.* (Cambridge University Press, 1987).

8 Tabor, D. *The hardness of metals.* (Oxford University Press).

9 Saurenbach, F., Terris, B.D. Imaging of ferroelectric domain walls by force microscopy. *Applied Physics Letters* **56,** 1703–1705, doi:doi:http://dx.doi.org/10.1063/1.103122 (1990).

10 Franke, K., Besold, J., Haessler, W., Seegebarth, C. Modification and detection of domains on ferroelectric PZT films by scanning force microscopy. *Surface Science* **302,** L283–L288, doi:http://dx.doi.org/10.1016/0039-6028(94)91089-8 (1994).

11 Setter, N. et al. Ferroelectric thin films: Review of materials, properties, and applications. *Journal of Applied Physics* **100,** 051606, doi:doi:http://dx.doi.org/10.1063/1.2336999 (2006).

12 Damjanovic, D. Ferroelectric, dielectric and piezoelectric properties of ferroelectric thin films and ceramics *Reports on Progress in Physics* **61,** 1267 (1998).

13 Nye, J.F. *Physical Properties of Crystals.* (Oxford University Press, 1985).

14 Magonov, S., Alexander, J., Wu, S. in *Scanning Probe Microscopy of Functional Materials* (eds Sergei V. Kalinin and Alexei Gruverman) Ch. 9, 233–300 (Springer New York, 2011).

Nanomeasurement Systems from Agilent Technologies

Agilent Technologies, the premier measurement company, offers high-precision, modular nanomeasurement solutions for research, industry, and education. Exceptional worldwide support is provided by experienced application scientists and technical service personnel. Agilent's leading-edge R&D laboratories ensure the continued, timely introduction and optimization of innovative, easy-to-use nanomeasure system technologies.

www.agilent.com/find/nano

Americas

Canada	(877) 894 4414
Latin America	305 269 7500
United States	(800) 829 4444

Asia Pacific

Australia	1 800 629 485
China	800 810 0189
Hong Kong	800 938 693
India	1 800 112 929
Japan	0120 (421) 345
Korea	080 769 0800
Malaysia	1 800 888 848
Singapore	1 800 375 8100
Taiwan	0800 047 866
Thailand	1 800 226 008

Europe & Middle East

Austria	43 (0) 1 360 277 1571
Belgium	32 (0) 2 404 93 40
Denmark	45 70 13 15 15
Finland	358 (0) 10 855 2100
France	0825 010 700*
	*0.125 € / minute
Germany	49 (0) 7031 464 6333
Ireland	1890 924 204
Israel	972-3-9288-504/544
Italy	39 02 92 60 8484
Netherlands	31 (0) 20 547 2111
Spain	34 (91) 631 3300
Sweden	0200-88 22 55
Switzerland	0800 80 53 53
United Kingdom	44 (0) 118 9276201

Other European Countries:
www.agilent.com/find/contactus

Product specifications and descriptions in this document subject to change without notice.

© Agilent Technologies, Inc. 2013

Published in USA, November 1, 2013
5991-3520EN

Agilent Technologies